ELSEVIER

Contents lists available at ScienceDirect

Materials Chemistry and Physics

journal homepage: www.elsevier.com/locate/matchemphys



Development of $NiCrFeCoB_X$ eutectic high entropy alloy coating by laser cladding: Investigation of microstructural, solidification, corrosion, and wear properties

Zhe Wu ^a, Morteza Taheri ^{b,*}, Kourosh Shirvani ^b, Edriss Raji ^c, Mohammad Javad Torkamany ^d, Reza Taghavi Jelodar ^e

- ^a School of Mechanical & Electrical Engineering, Xi'an Traffic Engineering Institute, Xi'an, Shaanxi, 710300, China
- b Department of Advanced Materials and New Energies, Iranian Research Organization for Science and Technology (IROST), Tehran, 33535111, Iran
- ^c Department of Materials and Metallurgical Engineering, Amirkabir University of Technology (Tehran Polytechnic), Hafez Ave., P.O. Box 159163-4311, Tehran, Iran
- ^d Iranian National Center for Laser Science and Technology, Tehran, Iran
- e Research Laboratory of NDE, Faculty of Materials and Industrial Engineering, Babol Noshirvani University of Technology, Mazandaran, Iran

HIGHLIGHTS

- NiCrFeCoBx high-entropy alloy was processed by laser cladding on a GTD-111 superalloy.
- Increasing B helps to refine the grains by causing non-heterogeneous nucleation.
- At B ≤ 0.4, the coating consists of interdendritic lamella pairing of FCC1, FCC2, and MXBY.
- An increase in B leads to a decrease in the corrosion current potential of the coating.
- Increasing B improves the tribological behavior with equiaxed grains.

ARTICLE INFO

Keywords: High entropy alloy Laser cladding NiCrFeCoB_X Microstructure Wear Corrosion

ABSTRACT

Developing protective coatings resistant to corrosion and wear has always been a challenge in various industries. In this work, we processed NiCrFeCoB $_{\rm X}$ (x = 0.1, 0.2, 0.3, 0.4, 0.5, 0.6) high-entropy alloy by laser cladding on a GTD-111 superalloy. At B \leq 0.3, the microstructure of the coating consisting of inter-dendritic FCC1 and FCC2 lamellae coupling was confirmed by XRD and SEM analysis. By increasing the value of B (B \geq 0.4), a coating with the phase structures of FCC1, FCC2, and M_XB_Y was identified. The presence of Cr-rich borides (M_XB_Y) was attributed to the enrichment of the eutectic composition with B and its segregation into interdendritic regions. With increasing B, more areas were created for inhomogeneous nucleation of dendrites from the melt, resulting in a finer eutectic structure with a higher volume fraction. The comparison between B0.1 and B0.6 samples showed that the hardness increased from 240 HV to 603 HV and the coefficient of friction decreased from 0.63 to 0.42. Raising the B value led to a drop in the corrosion current potential of the NiCrFeCoBX coating from -0.456 V to -0.895 V in a 3.5 % NaCl solution. Additionally, this shift altered the corrosion mechanism from pitting to intergranular corrosion. This was attributed to the high surface energy of the eutectic phase and the intensification of galvanic corrosion.

1. Introduction

Multi-element alloys, known as high entropy alloys (HEA_s), have attracted the attention of materials engineers in various industrial applications in the last decade because of their attractive properties [1].

Corrosion resistance, oxidation resistance, wear resistance, and high thermal tolerance are among the properties of HEAs [2]. It has been reported in the literature that HEAs that have multiphase structures have an excellent balance between toughness and ductility (in the case of rational design of phase compositions) [3]. HEAs that possess a

E-mail addresses: m.taheri@irost.ir, mtz.taheri@gmail.com (M. Taheri).

https://doi.org/10.1016/j.matchemphys.2024.129428

^{*} Corresponding author.

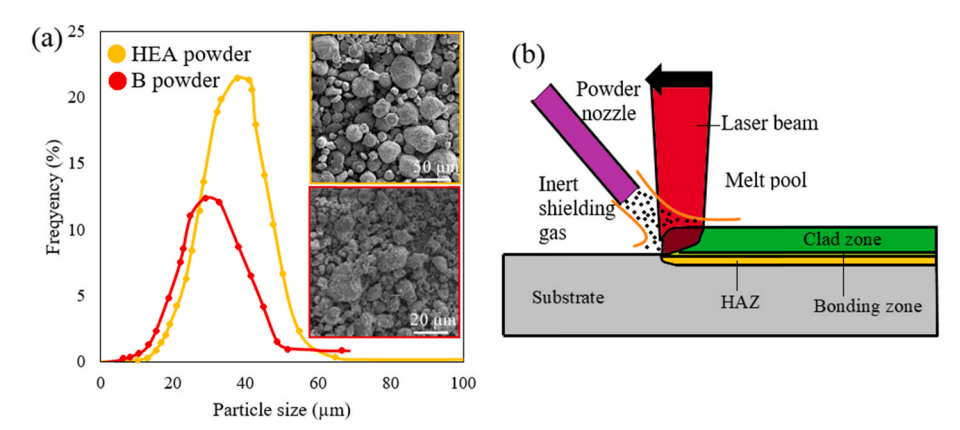


Fig. 1. (a) Particle size distribution of B and HEA powders, (b) Schematic representation of the LC process.

face-centered cubic (FCC) structure exhibit high ductility and low strength [4]. HEAs with FCC-HCP solid solution structures also have low ductility and high strength [4]. The low fluidity of HEAs and the tendency to severe segregation in melting processes are obstacles to their widespread use in the industry. Investigations have shown that HEAs with a structure close to the eutectic can overcome the mentioned limitations [5]. Lu et al. [6] in 2014 suggested the strategy of introducing HEAs with eutectic structure, which is a suitable solution to improve melt collapse and, of course, strengthen its microstructure. Therefore, it was suggested that the use of HEAs with a eutectic composition should be expanded. The design of HEAs with eutectic structures is mainly based on NiCrFeCo elements and the adding of elements with high electronegativity and atomic size differences such as Nb, Ta, Zr, and Hf [7]. In addition to the above metallic elements, small non-metallic elements can also contribute to the eutectic reaction because of significant property differences with intermediate metallic elements [8]. Although limited, the addition of small non-metallic elements such as C, B and, Si to some HEAs including NiCrFeCo has been reported in the literature [9, 10]. Among them, we can mention the HEAs of AlCoCrFeNi2.1 [6], CrFeNi2Al [11], and Al0.9CoFeNi2 [12]. It is reported in the literature that the addition of B to HEAs leads to the improvement of their mechanical properties such as strength, hardness, and wear resistance [13]. Boron can also help to stabilize the microstructure of the alloy, prevent the formation of undesirable phases, and increase its overall performance. In addition, B can also improve the high-temperature properties of HEAs, making them more suitable for use in extreme environments.

Vulnerability due to corrosion and wear of industrial parts has become a serious challenge in the introduction of materials for in various applications. One of the most influential and economical ways to increase the wear and corrosion properties of materials is to use surface engineering techniques. Laser cladding (LC) technology is a popular choice for creating corrosion and wear resistant coatings because of its low heat input, diverse parameters, high deposition efficiency, high quality metallurgical bonding, controllable thickness, and narrow heataffected zone (HAZ) [14,15]. As a result, in recent years, researchers and industrialists have paid considerable attention to LC. Various studies have suggested increased wear and corrosion resistance of HEAs with eutectic structures [16,17]. The hard-soft layers of the eutectic phase provide significant wear and corrosion resistance in addition to excellent ductility. Zhao et al. [18] produced an NbMoTaTiNi HEA coating processed by LC. Their research showed that the two-phase coating consists of (Ni) and NbMoTaTiNi phases, which is the main factor in improving

its tribological behavior. They also reported grain refinement, which is one of the characteristics of LC, to increase the wear resistance of the coating. Li et al. [19] investigated the corrosion behavior of NiCrCo-FeNbMoX (X = 0,0.25,0.5,0.75,1) HEA coatings applied by LC. Their findings indicated that the NiCrCoFeNbMo0.75 coating demonstrates superior corrosion resistance due to its significant presence of eutectic and lave phases. As Mo increased from 0.75, eutectics with refine layers were formed, which reduced the corrosion resistance of the coating. Deng et al. [20] prepared CoCrFeNi(TiNb)_{0.325} using a vacuum arc. The results of annealing the above alloy at 850 °C indicated the presence of needle-like L12 particles on a nanoscale and a remarkable increase in wear resistance. While annealing at 1160 °C indicated the removal of the eutectic phase and the reduction of hardness and wear resistance. Li et al. [21] processed the HEA AlCoCrFeNi_{2.1}/WC composite coating by LC. Their results showed that the resulting coating contains FCC and BCC phases. The highest hardness (572.3 HV_{1.0}) and wear resistance (average friction coefficient 0.535, as well as wear rate and wear volume reduction, respectively $4.4 \times 10^{-7} \text{ mm}^3 \text{N}^{-1} \text{ mm}^{-1}$ and 5.44 mm^3) were obtained with WC-30 %, which it was caused by the formation of Cr₇C₃ and Cr₂₁W₂C₆ phases. Xiang et al. [22] observed a high volume fraction of BCC phase along with Cr2Ti phase in the processing of CrFeNiTi and CoCrNiTi medium-entropy alloy coatings on Ti sheet. The presence of these phases caused a significant increase in wear resistance and hardness, which was caused by the short-range order, the combined reinforcing effect of the solid solution, and the refinement of the grains.

Presently, the primary focus of research on HEAs featuring eutectic structures revolves around the examination of microstructural characteristics, mechanical attributes, and hardening mechanisms within vacuum-melted block alloys [23]. The solidification mechanism and, of course, the determination of the eutectic melting point of HEAs are still not complete, which makes the rules of phase formation difficult. In this study, NiCrFeCoBx (x = 0.1, 0.2, 0.3, 0.4, 0.5, 0.6) HEAs were prepared by LC on the GTD-111 superalloy. After preparing the coating, a comprehensive analysis was performed on the phase composition, element, microstructure, and solidification mechanism of the prepared coatings to clarify the role of B on the properties of the coating. Finally, the relationship between the microstructure development and the corrosion and wear characteristics of the coatings was investigated and analyzed. It is expected that the development and realization of HEA coatings will expand their application in various industries.

Table 1 Chemical composition of GTD-111 superalloy (wt%).

Element	Co	Cr	Al	Ti	Ta	W	Nb	Mo	С	Ni
GTD-111	9.6	14.1	3.1	4.8	2.6	3.9	0.08	1.5	0.1	Bal.

Table 2
Laser cladding and ultrasonic parameters.

Average	Scan velocity	powder feed	hatch	laser beam
power (W)	(mm/s)	rate (mg/s)	distance (μm)	focus (µm)
200	7	300	80	100

2. Experimental procedures

GTD-111 Superalloy with dimensions of $60 \times 60 \times 2 \text{ mm}^3$ was used as the substrate. The microstructure and chemical composition of GTD-111 are presented in Fig. 1a and Table 1, respectively. Before the LC process, the GTD-111 surface underwent cleaning using sandpaper (to remove oxide and rust) and then acetone (to remove dirt and oil). NiCrFeCo aerosol powder and pure powder B (purity ≥99.9 %) were selected as coating materials. According to different molar ratios (X: 0.1, 0.2, 0.3, 0.4, 0.5, 0.6), powder B was mixed with NiCrFeCo powder in a ball mill at a speed of 360 r/min for 2 h. Finally, the resulting powder was placed in a drying oven (at a temperature of 120 °C for 1h) to remove any moisture. Fig. 1a shows the morphology and distribution of the powders used. To coat the HEA powders on GTD-111, the LC method was used. For this purpose, an IQL-10 pulsed laser with a maximum average power of 700 W was used. The parameters used for coating were selected based on trial and error and previous studies [18,24], which are presented in Table 2. A schematic of the coating process is shown in Fig. 1b. The clad zones (CZ_s) of different specimens in this research is called CZ-B0.1 \sim CZ-B0.6.

After finishing the coating, the specimens were cut by wire cutter to $2 \times 2 \times 2$ mm³ dimensions and after going through the metallographic

steps, including mounting, sanding (400# to 2000#), and polishing with alumina paste (with dimensions of 0.05 μm), for microstructural studies were prepared. After metallographic preparation, the specimens were etched with HCl: HNO3 =3: 1 etching solution for 20 s. The phase composition of the coating layer was identified by X-ray spectroscopy with experimental parameters ranging from 30° to 80° and scanning speed of $0.02^{\circ}/s$. A scanning electron microscope (SEM) equipped with EDS and EBSD was used to investigate the microstructure of the resulting coatings. An FEI Talos F200 field emission transmission electron microscope (TEM) was utilized to examine and analyze bright field and selected area electron diffraction (SAED) images with the assistance of DigitalMicrograph software.

To investigate the corrosion behavior, the specimens were immersed in 3.5 % NaCl solution, and their corrosion resistance was calculated using the LK98BII electrochemical workstation. The electrochemical test parameters were scan rate 0.5 mV/s, test potential -2 to 2 V, and working electrode area 1 cm². The wear test was performed using $\rm Si_3N_4$ ceramic with a diameter of 5 mm (upper wear specimen of friction pair) on HEA coatings (as friction pair). The rotation speed, opening, wear path diameter, and test time were 500 rpm, 100 N, 10 mm, and 20 min, respectively. The microhardness was measured using a load of 500 g for 10 s using the iVision-HV microhardness device. The microhardness values of the five locations were collected, and the average value was considered as the microhardness value of the coating layer.

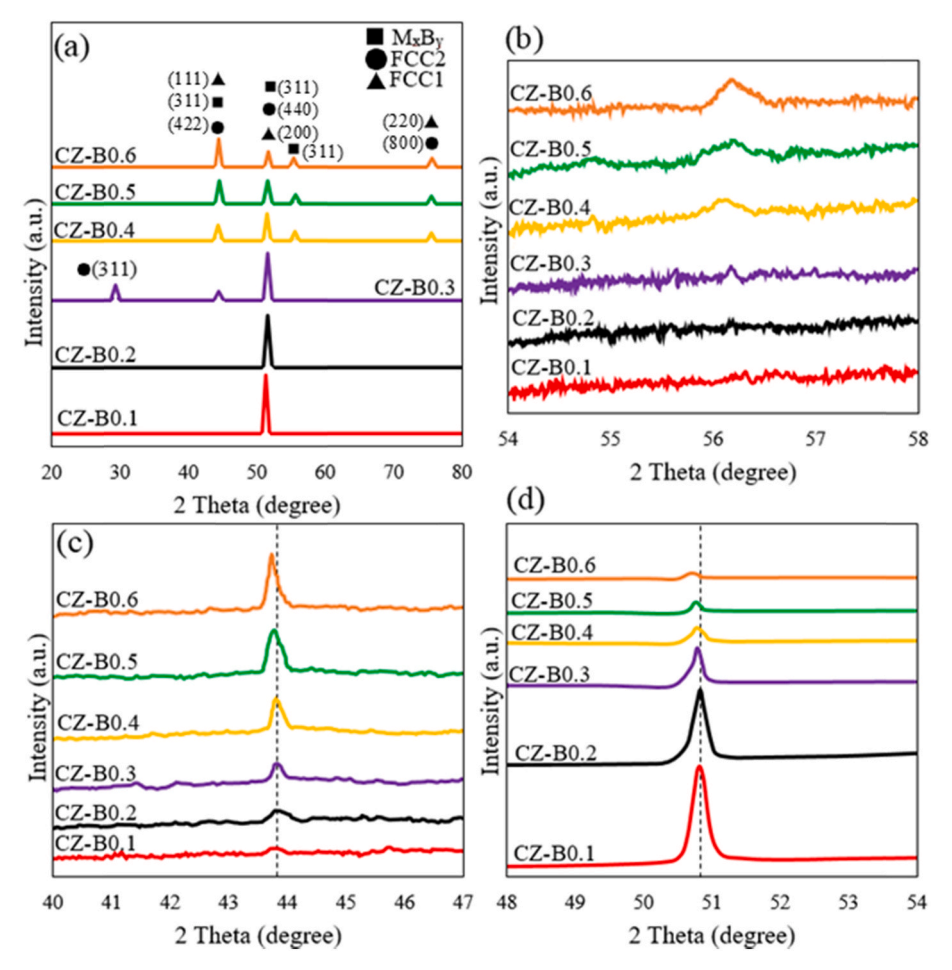


Fig. 2. (a) XRD patterns of HEAs coatings, (b) XRD patterns for the locally magnified view at $54 \sim 58$, (c) $40 \sim 47$, and (d) $48 \sim 54$.

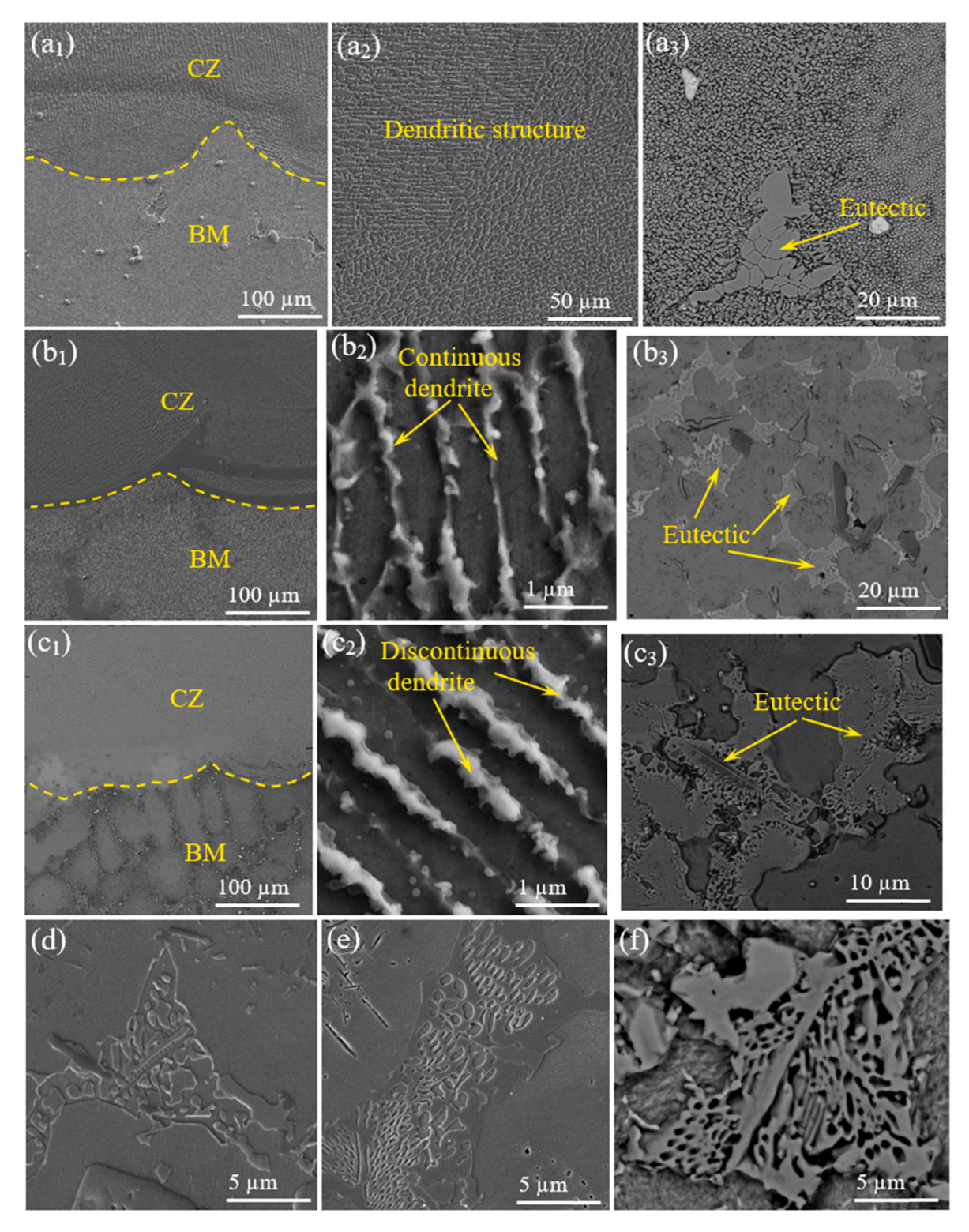


Fig. 3. SEM image of the cross-section of the coatings applied by the LC, (a) CZ-B0.2, (b) CZ, B0.4, (c) CZ-B0.6; (d) Magnified image of the eutectic of samples CZ-B0.2, (e) CZ-B0.4, and CZ-B0.6.

3. Results and discussion

3.1. XRD analysis

The results of XRD analysis of the coatings processed by LC are shown in Fig. 2a. As can be seen, the dominant microstructure of the coatings includes three FCC phases (FCC1, FCC2) and the M_XB_Y boride phase. In specimens where the B value is small, only two FCC phases are

formed in the coating. An extensive view of the XRD diagram in some important angles is shown at Fig. 2b–d. The diffraction angle between $54^{\circ}\text{-}58^{\circ}$ in Fig. 2b shows that with an increase in B, the diffraction peak of the M_XB_Y boride phase appears at 56.3° . The magnified views of angles $40\text{-}47^{\circ}$ (Figs. 2c) and $48\text{-}54^{\circ}$ (Fig. 2d) also show that as the value of B increases, the peaks related to the M_XB_Y phase are shifted to the left. The shift of the peaks to the left can be proved according to the Bragg relation (n $\lambda=2d\text{sin}\Theta$). According to this equation, the decrease in Θ is

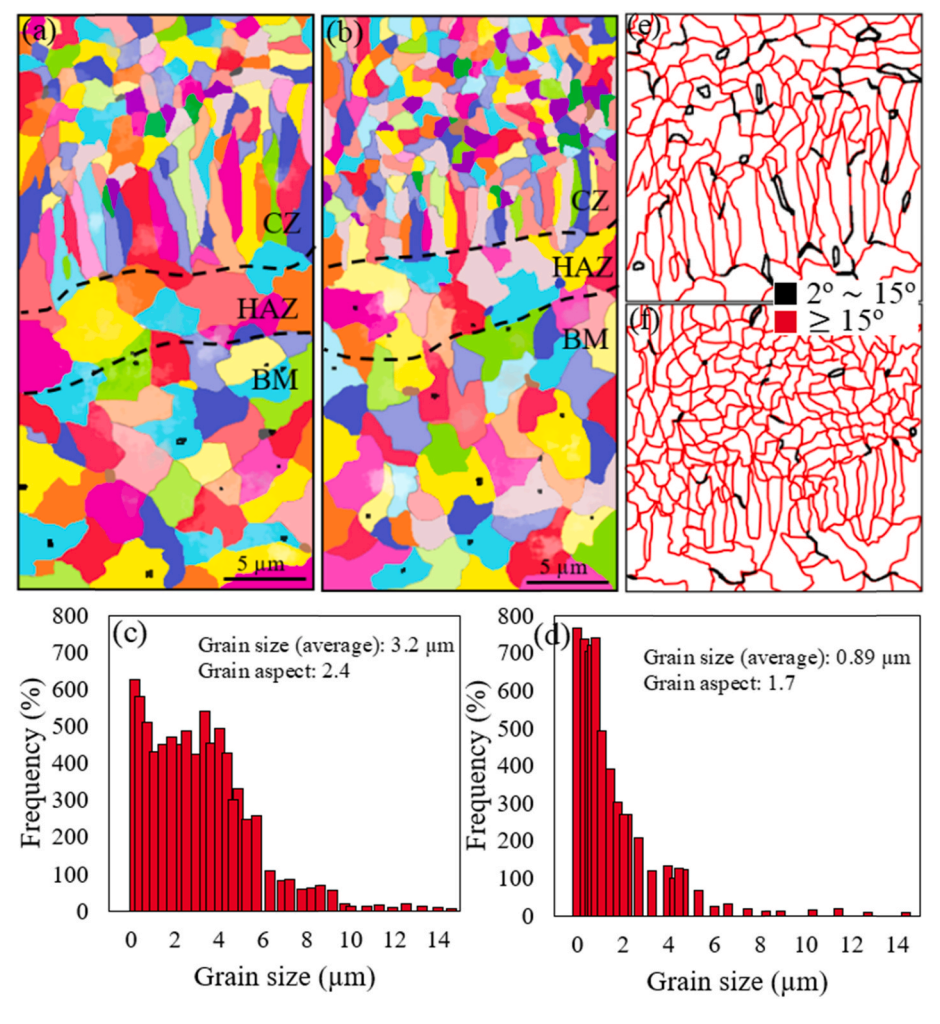


Fig. 4. (a) EBSD analysis of CZ-B0.1 and (b) CZ-B0.5 coatings; (c) The EBSD statistics of grain size in CZ-B0.1, and (d) CZ-B0.5 coatings; (e) corresponding grain boundary misorientation distribution figures of CZ-B0.1, and (f) CZ-B0.5 coatings.

attributed to the increase in the distance between the crystal planes, which is probably caused by the strengthening effect of B. In Fig. 2c, the peak intensity at 50.9° has reduced. Meanwhile, the intensity of the peak in Fig. 2d at an angle of 43.6° has experienced a noticeable decrease. It is stated in the literature that the peak intensity reflects the relative content of the phase to some extent [25]. It is concluded that with increasing B, the FCC1 peak decreases with a diffraction peak of 50.9°, while the FCC2 phase increases with a diffraction peak of 43.6°. Under the conditions where the values of B are 0.1 and 0.2, the crystal planes were dominant (440) and (200), and there was a distinct crystal alignment of the crystals in the coating. With an increase in the content of B, the preferred orientation of the crystal planes (440) and (200) attenuation and the direction of the crystal planes (111) and (422) increase. This confirms that with an increase in the B value, the FCC1 and FCC2 phases decrease and increase, respectively. In the literature, three phases (FCC1, FCC2, and M_xB_y) have been reported in the melting of NiCrFe-CoB_X HEA_S [26]. The results of this research showed that the number of peaks, especially those related to MxBy, is less than the mass melting of NiCrFeCoB_X HEA_S. This is attributed to non-equilibrium solidification of the coating due to fast solidification in the LC and increased cooling rate at high B values. Under such conditions, the formation of additional compounds and the segregation of alloy elements are suppressed.

3.2. Microstructural investigations

SEM images of the microstructure of the resulting coatings on the

GTD-111 superalloy are shown in Fig. 3. As can be seen, the coatings are uniformly deposited on the substrate with proper overlap and without any defects. Microstructural investigations showed that the average thickness of the coating is about 383 \pm 27 μm . So with the increase of B value, the tendency to decrease the thickness somewhat increases. The above figures show that the dominant structure of the coatings is dendritic. Closer examination at higher magnification also indicates that the growth orientation of the dendrites weakens as more B is added. In addition, with the addition of B, the dendrites became shorter and thinner, and their volume fraction decreased. The reason for these changes is the addition of B. With the addition of B, the cooling rate first increases, because B acts as an inhomogeneous nucleation center and increases the solidification rate. Under such conditions, the dendrites become shorter and finer. Second, element B facilitates the formation of eutectic structures. These structures were observed in the inter-dendritic regions, particularly in the CZ-B0.5 and CZ-B0.6 specimens. It has been reported that eutectic structures grow in the interdendritic regions using the synthetic crystallization method [27]. In addition to the dendritic structure, a comparison of the EBSD images of CZ-B0.1 with those of CZ-B0.5 in Figs. 4a and b shows that the CZ region has more refined grains than the base metal region. This issue is more noticeable in the case of the CZ-B0.5 specimen. As mentioned earlier, with increasing B, the cooling rate, the tendency to form a finer eutectic, and the eutectic volume fraction increase. In addition, Figs. 4e and f shows that the CZ-B0.5 specimen has fewer low-angle grain boundaries (LAGB) (black lines) and more high-angle grain boundaries (HAGB) (red lines) than the

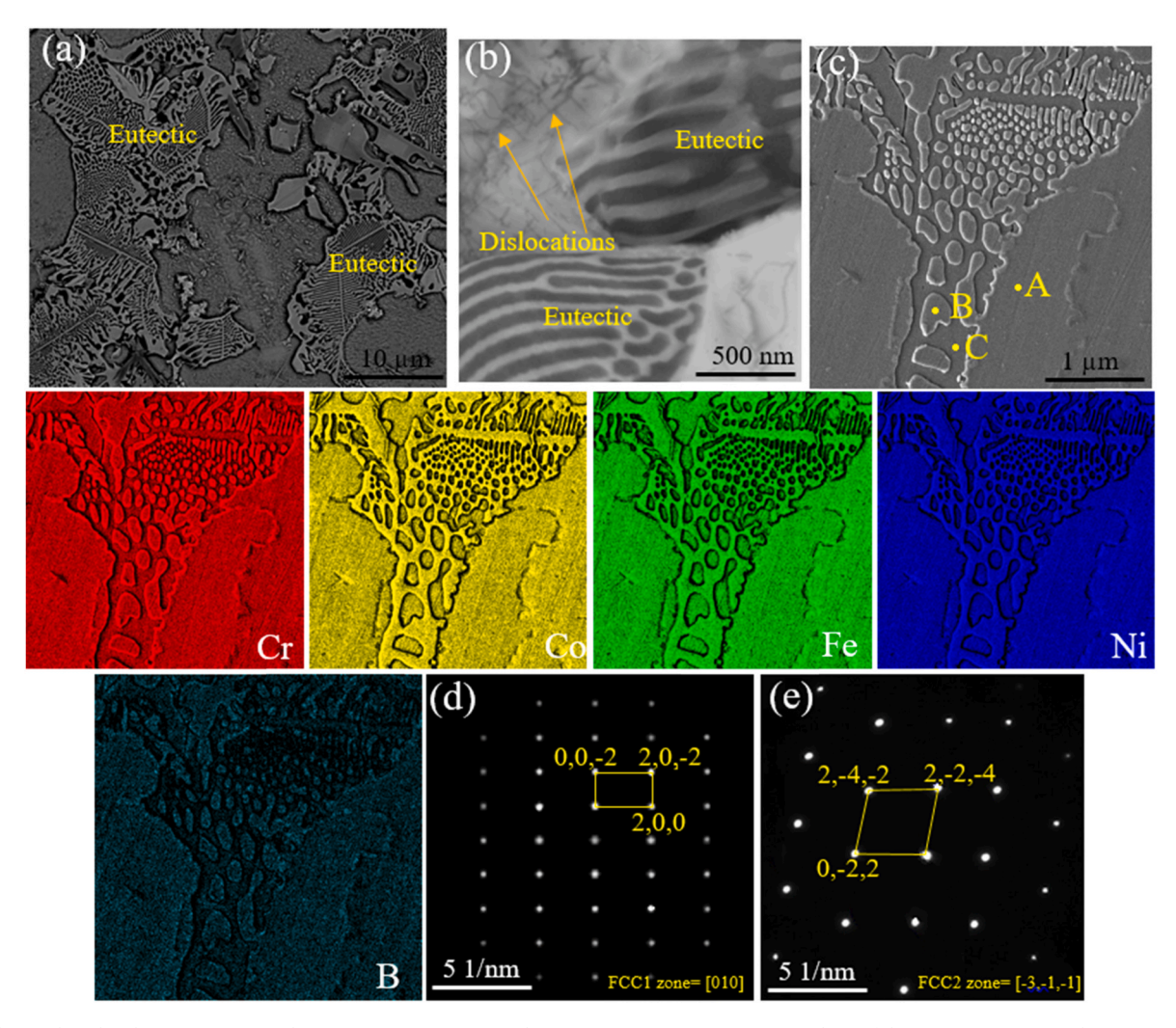


Fig. 5. The results related to CZ-B0.2T sample, (a) SEM microstructure, (b) TEM microstructure, (c) Map analysis of the eutectic structure, (d) SAED pattern of the point A and B, (e) SAED pattern of the point C.

Table 3The results of the EDS analysis of the marked points in Fig. 5c.

Point	Cr	Co	Ni	Fe	В
A	51.76	14.72	5.76	17.61	10.15
В	23.79	16.48	31.35	25.17	3.21
C	21.05	24.34	25.67	27.59	1.35

CZ-B0.1 specimen. The grain boundaries of specimen CZ-B0.5 grow in a zigzag pattern. It has been reported that zigzag grain boundaries increase the toughness of materials by preventing crack propagation [28]. In addition, another report states that LAGB is a place for the accumulation of elements that reduce the melting point, which is the result of increased sensitivity to hot cracks [29]. The grain distribution histogram in Figs. 4c and d shows that the average grain size for specimens CZ-B0.1 and CZ-B0.5 decreased from 3.2 μm to 0.89 μm . The same is true for the grain ratio (2.4 vs. 1.7). The average grain size in the sublayer was 9.5 μm , which indicates that the sublayer acts as a heat sink during LC and remains unchanged. The increase in grain size in the HAZ is also caused by the increase in heat input; therfore, the average grain size in the HAZ was reported as 10.7 μm .

Fig. 5a and b shows the SEM and TEM images of the CZ-B0.2 sample, respectively. As can be seen in both images, the coating consists of two separate parts that include dendrite core regions (DCR) and interdendritic regions (IDR) that include layered eutectic. The magnified

Table 4 The enthalpies of mixing for binary compounds of elements ΔH_{AB}^{mix} .

Elements	Ni	Cr	Fe	Co	В
Ni	-				-25
Cr	-6	_	-1		-29
Fe	-2		-		-27
Co	0	-4	-1	-	-25
В					-

area of the marked image in Fig. 5b shows some crossed dislocation lines. The presence of these lines is attributed to the tensile stresses generated during rapid solidification during LC processing [30]. The results of the EDS map of the eutectic in Fig. 5c show that Cr has the highest concentration in the eutectic. Meanwhile, element B is not very significant because of its overall concentration. The results of the EDS analysis of point A in Table 3 show the richness of Ni, Cr, Fe, and Co elements with almost equal ratios and poorness in B element. At point B, the eutectic zone is layered and is located in the IDR. Two points B and C are isolated. As shown in the results in Table 3, point C can be called the Cr-rich phase. The analysis of point B has almost the same composition as that of point A, except that it contains a lower amount of Cr. The calculation results of mixing enthalpies of ΔH_{AB}^{mix} in Table 4 (calculated based on the Miedema model) show that elements Cr and B have the most negative mixing enthalpies, which facilitates the formation of

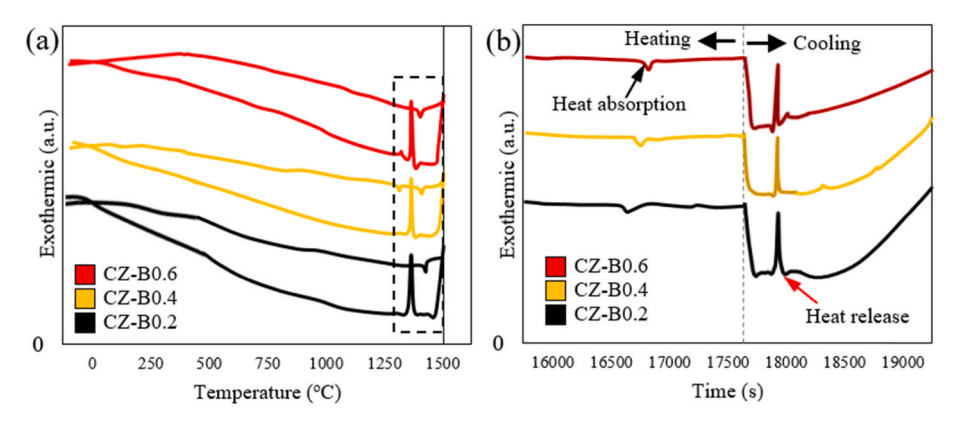


Fig. 6. DSC curves of the B0.2, B0.4, and B0.6 mixed powders.

Table 5 Fitting parameters of DSC curves.

Coating	CZ-B0.2	CZ-B0.4	CZ-B0.6
Start melting temperature (°C)	1417.22	1419.08	1431.05
Complete melting temperature (${}^{\circ}C$)	1432.57	1433.21	1448.71
Melting enthalpy (J/g)	-47.95	-38.32	-50.11
Start solidification temperature (${}^{\circ}C$)	1422.57	1416.77	1415.77
Complete solidification temperature (${}^{\circ}C$)	1402.25	1397.88	1395.91
Solidification enthalpy (J/g)	+93.58	+60.11	+56.42

stable compounds through the combination of these two elements. The results of the SAED analysis also confirmed this. As shown in Fig. 5d, points A and B have the same disordered FCC phase. The SAED analysis results in Fig. 5e show that point C has a separate and Cr-rich ordered FCC phase. According to the XRD results, it can be concluded that the poor compounds in B–Cr belong to the FCC2 phase and the other phase to FCC1.

3.3. Analysis of differential scanning calorimetry and solidification

Fig. 6 shows the DSC diagram of the NiCrFeCoB $_{0.2.0.4\ and\ 0.6}$ powders. As can be seen, from about 500 $^{\circ}C$ to the end of powder melting, the DSC semi-parabolic curve of all specimens experiences a decreasing path. The declining pattern of the curves intensifies as the temperature and time progress towards the melting zone, suggesting the initiation of an endothermic process before the powders fully melt, attributed to the rise in the specific heat of the HEA powders as the temperature increases. Likewise, after melting the powders and during solidification, the heat of the HEA powders also decreases. Between 1300 °C and 1500 °C, there is a local increase in temperature. To clarify this issue, the thermodynamic parameters of powders B0.2, B0.4, and B0.6, derived from fitting and integrating the solidification endothermic peak with the melting endothermic peak, are outlined in Table 5. According to the results in Fig. 6b and Table 5, the melting point increases with increasing B content. As per the theoretical calculation of the melting point of HEAs [31], the predicted melting temperatures for powders B0.2, B0.4, and B0.6 are 1602.5 °C, 1634.5 °C, and 1665.7 °C, respectively. Practical and

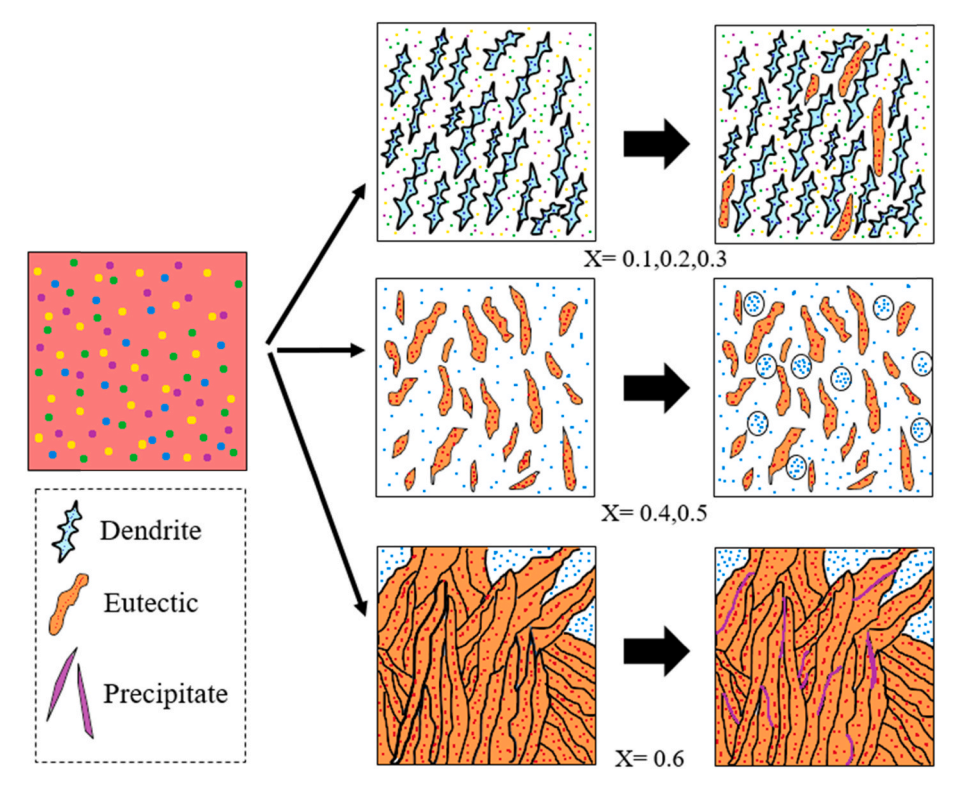


Fig. 7. Schematic diagram of crystallization and solidification process of laser coating of NiCrFeCoB_X coating.

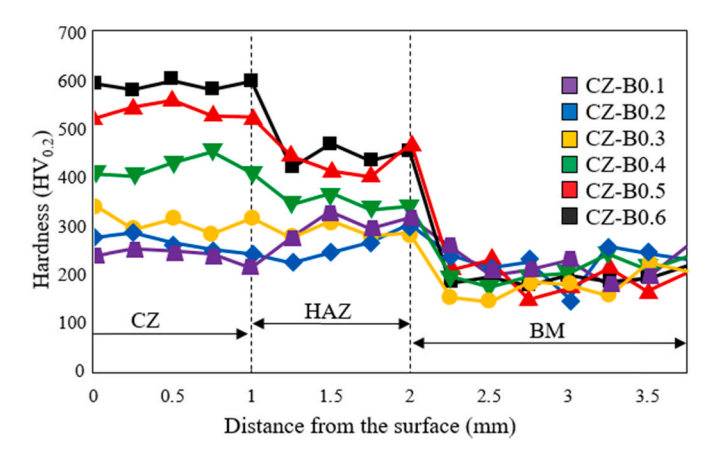
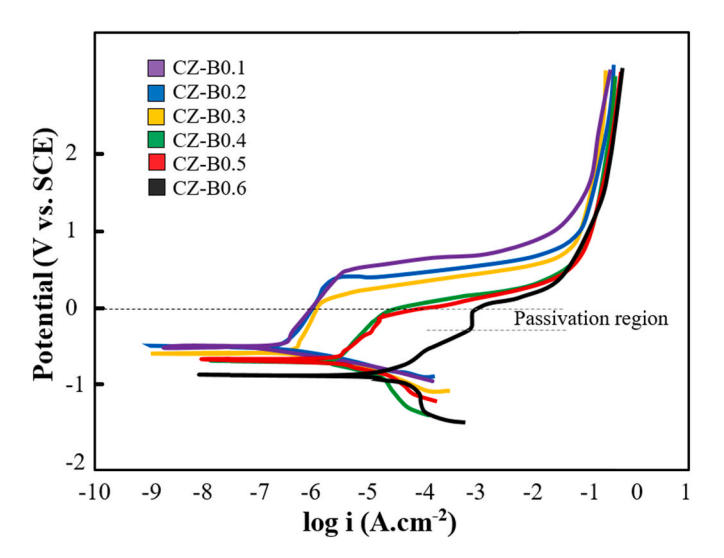


Fig. 8. Hardness results of NiCrFeCoB_X coatings.

theoretical melting points are indeed different, but their process are similar. The results show that by adding B, the melting point of the coatings becomes more significant. According to the general Gibbs free energy of the reaction, the enthalpy change during solidification is higher than that of melting for any powder, indicating that the reaction consistently transitions from a high-energy state to a low-energy state [32]. The melting enthalpy of the B0.6 powder in the exothermic process is higher than its solidification enthalpy in the exothermic process. This theory validates the unavoidable occurrence of a solid phase transformation in the B0.6 powder. The single crystallization peak of specimen B0.4 during solidification indicates that only one phase transition occurs during solidification. Therefore, the eutectic reaction occurs in the solidification temperature range when $B \leq 0.4$. However, two crystallization peaks were observed during the solidification of the B0.6 powder. This shows that after the end of solidification at the temperature of 1384.2 °C, the coating undergoes a solid-state phase transition. On the basis of the XRD and microstructural results, it can be assumed that band deposits are formed in the middle of the eutectic phase under such conditions. (See Fig. 5a).

The total results of XRD, microstructure, and DSC as well as what is mentioned in the literature about LC [28,29] show that the solidification of the resulting coatings in this research was non-equilibrium. For this purpose, the diagram in Fig. 7 shows a schematic of the solidification process of HEAs during LC. Under conditions where the B content is low (B0.1), the sites necessary for solidification nucleation are few. As a result, the driving force for solidification is created only from the cold walls of the sublayer. Under such conditions, elongated dendrites and a column (non-equiaxed) grow in the direction of the temperature gradient. With the segregation of B and its amount reaching the eutectic composition, a eutectic structure consisting of two FCC1 and 2FCC phases is formed with a layer pair distribution at low temperatures. When the B content is 0.2-0.3, a composition similar to that of the B0.1 coating is formed, but with a smaller microstructure (smaller grains and dendrites). This is attributed to an increase in the number of solidification nucleation sites. However, with the rise of B, the coating melt composition is closer to eutectic, and thus the dendritic structure gives way to the dominant eutectic structure. When the content of B is 0.4 and 0.5, the above conditions are stable. Eutectic reactions generally occur during the last moments of solidification. The increase in nucleation sites has caused the eutectic morphology to undergo changes similar to those in crab cactus. With the growth of the eutectic phase, the surrounding liquid, which was poor in element B and far from the eutectic composition, formed the FCC1 phase. As the content of B increases to 0.6, the melt composition goes beyond the eutectic composition. Under such conditions, excess element B is repelled into the remaining melt, and some of it is also dissolved as a solid in the eutectic. By decreasing the temperature and reaching 1384.2 °C, a phase transition occurred in the solid state in B-enriched eutectics, which resulted in the



 $\textbf{Fig. 9.} \ \ \textbf{Potentiodynamic polarization curves of NiCrFeCoB}_{X} \ \ \textbf{coatings.}$

precipitation of strip-shaped borides.

3.4. Microhardness results

Fig. 8 shows the microhardness results of different specimens. As can be seen, the average hardness of the coating in all specimens has increased significantly compared to the substrate with an average hardness of 208 HV. The increase in hardness compared with the substrate was at least 18 % for the B0.1 specimen and at most 180 % for the B0.6 specimen. Therefore, as is clear from the graph, with an increase in B, the hardness value increases. The reason for this, as mentioned, was the smaller dendrites and grains of the coating structure with increasing B value (see Fig. 4). However, the difference in the atomic radius of Ni, Cr, Fe, and Co increases the hardness of the HEA coating by causing lattice distortion. In addition, the addition of element B to HEA due to its smaller atomic diameter increases the hardness of the HEA coating by increasing the tendency to form a solid solution. In addition, lattice distortion during LC, which strengthens dislocation defects, increases the hardness of HEAs [5-7]. Xiang et al. [33] reported that the presence of Ti in the solid solution phase in CoCrFeNiNbx coatings processed by laser cladding inevitably causes large lattice distortions and subsequent hardness and strength due to significant differences in atomic radius between them. Another research study indicated that the strong negative enthalpy of mixing between B and elements like Cr and Fe leads to the creation of intricate boride phases, contributing significantly to the enhancement of hardness [34]. Hardness values in the HAZ are lower than in CZ and higher than in the base metal (BM). In general, the decrease in hardness in the HAZ, which is attributed to the lack of grain refinement, was not far from expected. However, the possibility of penetration of a small amount of HEA elements from the CZ to the HAZ increases the hardness of the HAZ compared to the BM [35]. The creation of residual stresses due to rapid cooling is one of the other factors contributing to increased hardness in the HAZ [36]. However, the difference in hardness in the HAZ of different specimens can also be attributed to the solidification rate in the CZ. In specimens with high B content (such as CZ-B0.5 and CZ-B0.6), where the cooling rate of the CZ is very fast, the cooling rate in the HAZ also increases. As a result, in addition to increasing residual stress, the opportunity for grain growth is limited. In specimens with low B content (such as CZ-B0.1 and CZ-B0.2), due to the lower solidification speed, the HAZ region will experience fewer residual stresses and, of course, more grain growth.

Table 6 Electrochemical parameters of NiCrFeCoB $_{\rm X}$ coatings in 3.5 wt% NaCl solution.

Coatings	CZ-B0.1	CZ-B0.2	CZ-B0.3	CZ-B0.4	CZ-B0.5	CZ-B0.6
E _{corr} (V) I _{corr} (A/ cm ²)	-0.456 1.256×10^{-6}	-0.459 1.357×10^{-6}	-0.573 1.696×10^{-6}	$-0.621 \\ 1.851 \times \\ 10^{-6}$	-0.625 1.887×10^{-6}	-0.895 3.594×10^{-6}

3.5 Corrosion test results

The corrosion test results, including the potentiodynamic polarization curves of the CZ-B0.1 \sim CZ-B0.6 coatings in 3.5 % NaCl solution, are shown in Fig. 9. According to the literature, it is mentioned that a higher self-corrosion potential (Ecorr) and a lower self-corrosion current density (I_{corr}) are indicative of superior corrosion resistance of the material. The findings indicate that as the B content increases, the dynamic polarization curves of the coatings shift downwards and to the right. The results of fitting this curve are also presented in Table 6. As is clear, with the addition of B, E_{corr} decreased from -0.456 for the CZ-B0.1 coating to -0.895 for the CZ-B0.6 coating. Meanwhile, the Icorr increased from 1.256×10^{-6} for CZ-B0.1 coating to 3.594×10^{-6} for CZ-B0.6 coating. As the potential increases, the self-corrosion current density increases steadily in the anodic polarization region. As the potential increases, I_{corr} steadily increases in the anodic polarization region. This causes a large amount of the coating material to dissolve as metal cations in the electrolyte solution. As the potential increases up to approximately $-0.14 \, \text{V}$, the Icorr of the CZ-B0.6 coating decreases slightly, which is attributed to a reaction and the formation of a passive film in a particular potential range. This film significantly reduces the corrosion rate of the coating, a topic that has been documented in several studies as well [37]. As the potential increases and reaches approximately -0.38 V, the passive layer is broken, and as a result, its protective effect on the anode metal gradually disappears. It enters the activation zone, which is the metal dissolution zone. Nevertheless, the electrochemical corrosion performance of the coating excels over other coatings when the B content is high.

In order to check the corrosion results more accurately, the analysis was conducted on the fitting outcomes of the electrochemical impedance spectrum (EIS) for the different CZ-B0.1 \sim CZ-B0.6 samples. Fig. 10a shows the equivalent circuit of different coatings. As can be seen, this equivalent circuit includes components of charge transfer resistance (Rct), solution resistance (Rs), and constant phase angle element Q (CPE). The single capacitive arc impedance diagram in Fig. 10b also shows that at high values of B (such as CZ-B0.6 coating), the impedance and capacitive arc are transferred to lower values. The

parameters for the equivalent circuit elements have been detailed in Table 7. The value of R_s is much less than that of R_{ct} . However, the R_{ct} values of the CZ-B0.1 \sim CZ-B0.3 coatings are on the megaohm scale. As can be seen, with an increase in the B content, the corrosion resistance gradually decreases, as shown in Fig. 10. The scattering coefficients Q (n) obtained from the EIS fitting are at most 0.7, which indicates that the coating surfaces are very dense.

Fig. 10c shows the Bode results for the CZ-B0.1 \sim CZ-B0.6 coatings. The impedance modulus |Z| indicates the combined values of R_s and R_{ct} at lower frequencies. Meanwhile, in the high-frequency range, |Z| represents Rs. As can be seen, as the content of B increases, the impedance of the coatings decreases. The diagram for the CZ-B0.6 coating shows a low-capacitance but high-resistance insulating layer with a broad phase plateau in the mid-frequency range. This region corresponds to the inactive region shown in Fig. 9 (dynamic polarization curve). While the CZ-B0.6 coating can be rendered inactive in a 3.5 % NaCl solution, its corrosion resistance is lower due to its reduced impedance when compared to alternative coatings.

Fig. 11 shows the morphology of the corrosion coatings. The morphology of specimen B0.1 shows pits on its surface after corrosion, which have a rough interior. This issue indicates almost severe pitting corrosion. As per reports, High-Entropy Alloys (HEAs) are susceptible to pitting corrosion when the electrolyte solution includes reactive chloride (Cl⁻) anions [38]. After corrosion, the eutectic structures are less visible. As can be seen, with an increase in B, the content of pits decreased. Magnification of the pits shows that the skeleton of the eutectic structure is preserved inside the pits. With an increase in the B content, intergranular corrosion occurred. Therefore, in specimens CZ-B0.3 and CZ-B0.4, the highest amount of intergranular corrosion occurred. Intergranular corrosion, but of uniform type, can also be seen

Table 7Parameters of equivalent circuit fitting.

Coatings	CZ-B0.1	CZ-B0.2	CZ-B0.3	CZ-B0.4	CZ-B0.5	CZ-B0.6
$R_s(\Omega)$ n_1	7.254 0.9549	7.854 0.8854	8.651 0.8621	8.021 0.8599	7.058 0.9115	2.3218 0.7657
Q ₁ (S. sec ⁿ)	1.985×10^{-5}	2.214×10^{-5}	2.544×10^{-5}	3.112×10^{-5}	4.854×10^{-5}	1.746×10^{-4}
$R_{ct1}(\Omega)$	4.652×10^{6}	3.028×10^{6}	6.874×10^{6}	5.351×10^{6}	1.871×10^{4}	8419
n ₂ O ₂ (S.				0.716 9.245 ×	0.854 8.568 ×	1 4.621 ×
sec ⁿ)				10 ⁻⁵	10 ⁻⁶	10^{-6}
R _{ct2} (Ω)				5.982 × 10 ⁴	4.146 × 10 ⁴	3.165

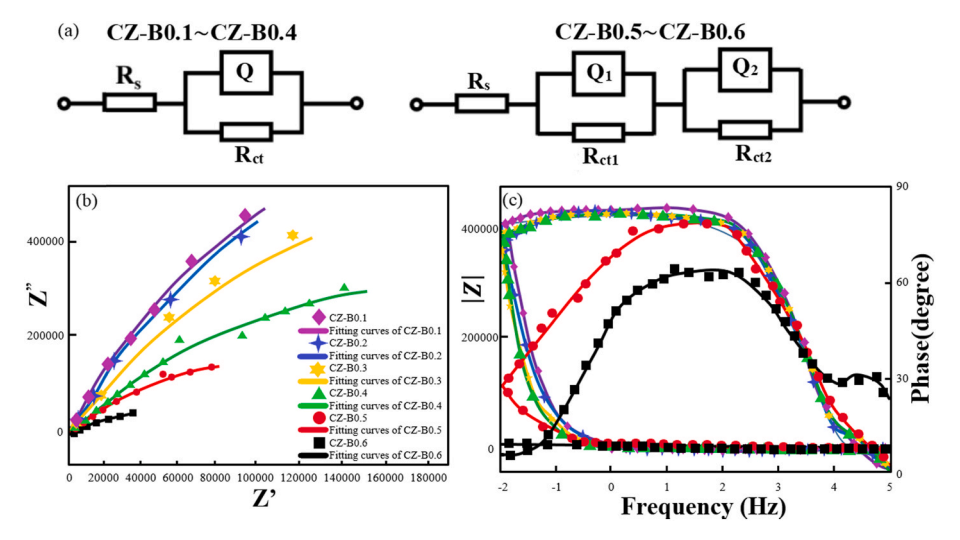


Fig. 10. EIS analysis curve, (a) equivalent circuit curves, (b) Nyquist plots, (c) Bode curves.

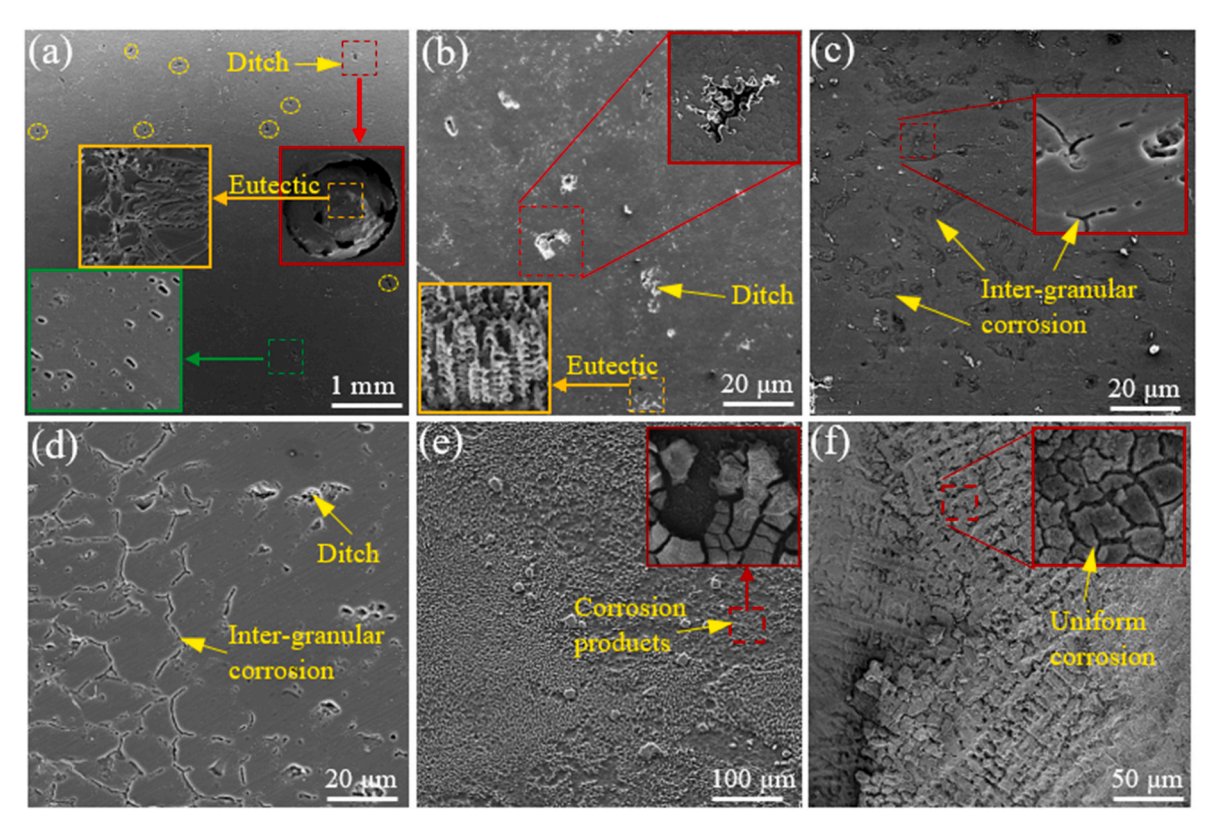


Fig. 11. Corrosion morphologies of NiCrFeCoB_X coatings, (a) CZ-B0.1, (b) CZ-B0.2, (c) CZ-B0.3, (d) CZ-B0.4, (e) CZ-B0.5, (f) CZ-B0.6.

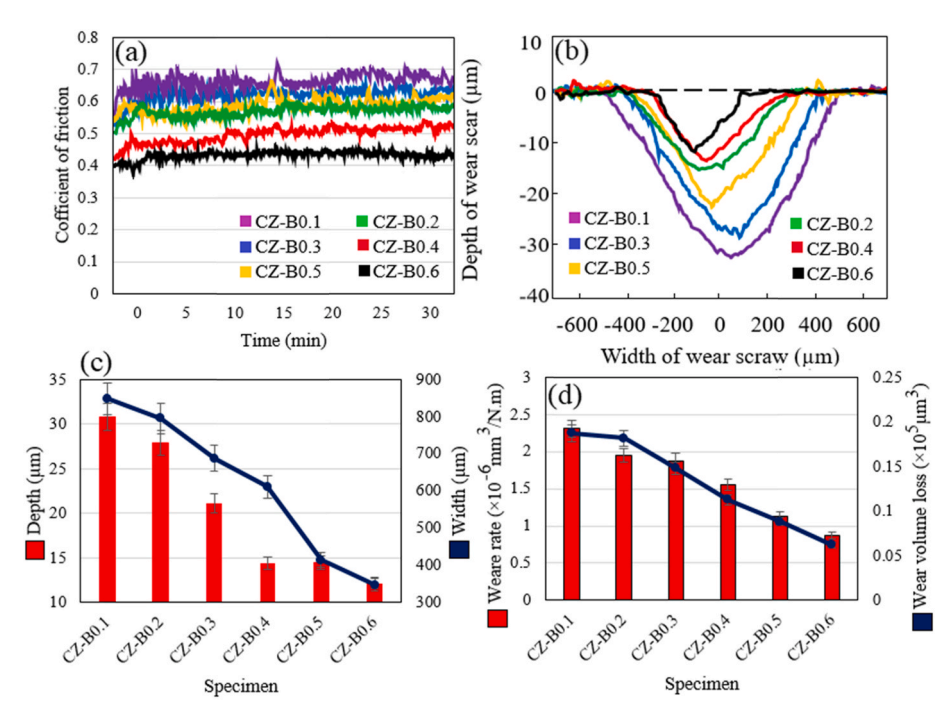


Fig. 12. Results of wear test, (a) Cofficient of friction, (b) Depth of wear, (c) average of depth and width wear, (d) Wear volume loss and wear rate.

in the CZ-B0.5 and CZ-B0.6 specimens. The cracks in the corroded veins are related to boride phases rich in Cr (see Fig. 7). In the high-magnifications images, corrosion of the eutectic layers that have the appearance of freezing is also observed in the structure of the specimens. There are many interphase boundaries between the coupled lamellae of phases FCC1 and FCC2 in the eutectic structure. These boundaries are high-energy areas that are highly prone to corrosion.

Phase FCC2, which has a high Cr has a high potential difference from phase FCC1, which strongly encourages galvanic corrosion. This issue causes the dissolution of phase FCC1 and the appearance of the skeletal structure of phase FCC2. In general, with an increase in B, the volume fraction of the eutectic phase increases, and as a result, the tendency for intergranular corrosion increases. The presence of the broken film in Fig. 11e and f corresponds to the fractured inactive film on the CZ-B0.5

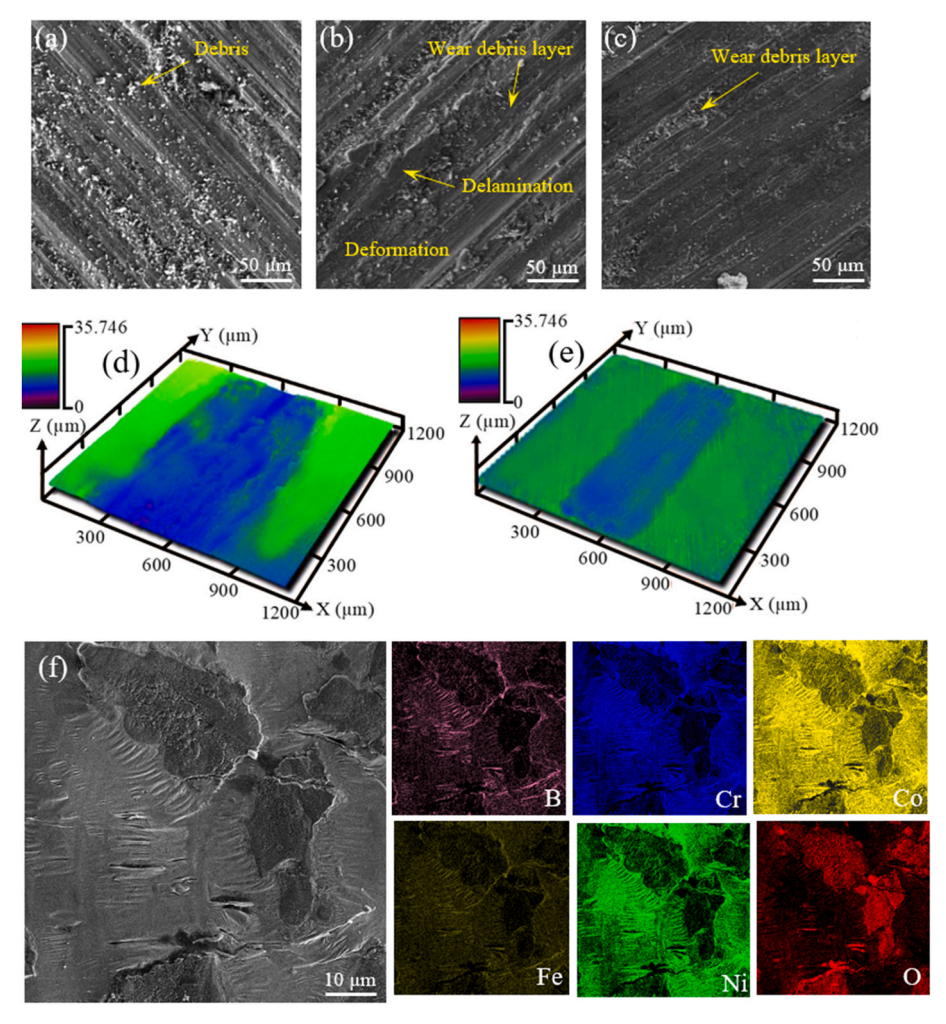


Fig. 13. SEM of the worn surface of NiCrFeCoB_X HEAs: (a) CZ-B0.1, (b) CZ-B0.3, (c) CZ-B0.6; 3D-profilometer of the worn surface: (d) CZ-B0.1, (e) CZ-B0.6, (f) EDS mapping of worn surfaces of CZ-B0.1.

and CZ-B0.6 coatings. This film is associated with the passive region of the polarization curve of the CZ-B0.6 coating, which has a suitable protective effect to prevent electrochemical corrosion.

3.6. Wear test results

Fig. 12a shows the changes in the coefficient of friction (COF) with time for the CZ-B0.1 \sim CZ-B0.6 specimens. According to the above figure, the friction and wear process can be categorized into two phases: initial wear and steady wear. During the initial wear phase, the coefficient of friction rises due to the interaction between the specimen surface and the Si3N4 friction ball under a specified load. By increasing the contact between the ball and the surface of the specimen, the point contact turns into a plane contact, and as a result, the stable wear stage begins, and, the upward trend of COF stops [39]. According to Fig. 12a, it can be seen that with an increase in B, the stability of COF increases. This is attributed to greater grain refinement in the CZ layer, which is an advantages of LC. In addition, with the rise of B, the number of complex phases of FCC1, FCC2, and boride increases (increase of eutectic phase). This has also helped to reduce COF.

To better understand the wear results, the wear depth was investigated in different specimens (Figs. 12b and c). The above results show a trend similar to that of COF. Therefore, a CZ-B0.1 specimen with COF 0.63 and a wear depth of 31.1 μm was the weakest, and the CZ-B0.6 coating with COF 0.42 and a wear depth of 12.5 μm showed the best wear resistance. According to the results, the reduction in the wear rate

of the CZ-B0.6 specimen shown in Fig. 12d was not far from that expected. Therefore, the CZ-B0.6 coating with a wear rate of $0.78\times10^{-6}~\text{mm}^3/\text{N.m}$ showed the best wear behavior, and the CZ-B0.1 specimen with a wear rate of $2.41\times10^{-6}~\text{mm}^3/\text{N.m}$ showed the weakest wear behavior.

To investigate the complex effect of the microstructure on the wear mechanism during the dry sliding test, Fig. 13a-c shows the morphology of the worn surfaces after the wear test. As can be seen, with an increase in B, the wear debris decreased in size and number. Therefore, the CZ-B0.6 specimen has the smoothest surface. Fig. 13d and e also show that the size of the hook grooves also decreased (according to the results of Fig. 12b-c). The large debris generated in Fig. 13a (CZ-B0.1) may adhere to the previously worn surface and thus form relatively large piles. Deng et al. [19] reported that the above particles may decompose and remove surface roughness during continued wear. SEM images of worn surfaces show that most specimens have experienced the delamination phenomenon. This process intensifies with decreasing B. EDS map analysis of the magnified adhesive layer in specimen CZ-B0.1 (Fig. 13f) shows that the upper layer is rich in O. The traces of plastic deformation and scratches on the adhesive layer show that the above layer is distinct from the surface material and the oxide film. The presence of the above layer is attributed to the heating caused by the friction between the surface and the sliding ball. It is stated in the literature that the above temperature increase, which is known as flash temperature, can reach up to 800 °C and the temperature around it can reach up to 500 °C [40]. The oxidation resulting from the flash temperature also softens the waste particles, which further increases the fluctuation in COF as the particles harden. The strong fluctuation of the specimens with low B in Fig. 12a, especially at early times, is attributed to this. Chai et al. [41] report showed that the high hardness of CrNiTi medium-entropy alloy coating processed by laser cladding causes the transfer of Si from $\rm Si_3Ni_4$ ceramic balls and its spalling during the wear test.

4. Conclusion

In this study, high entropy coating of NiCrFeCoB $_{\rm x}$ (x = 0.1,0.2,0.3,0.4,0.5,0.6) was successfully performed by LC, and the following results were obtained.

- 1. The NiCrFeCoB $_{x}$ coating with B \leq 0.3 was two-phase and had a structure consisting of the pairing of FCC1 and FCC2 lamellae. With increasing B (B \geq 0.4), the Cr-rich boride phase (M $_{x}$ B $_{y}$) appeared in addition to FCC1, FCC2. The reason for this was that element B exceeded the eutectic composition limit.
- 2. With the increase of B content, the structure of dendrites was inclined from columnar and cellular to equiaxed. The reason for this was the increase in inhomogeneous nucleation of B atoms in the melt, which caused the refinement of grains. Of course, the role of the LC process in the rapid solidification of the coating cannot be ignored.
- 3. Increasing the content of eutectic and the fineness of grains in high contents of B, causes a significant increase in the coating hardness from 221 HV $_{0.2}$ (CZ-B0.1) to 603 HV $_{0.2}$ (CZ-B0.6), reducing the COF from 0.63 to 0.42, and a decrease in the wear rate from 2.41 \times 10 $^{-6}$ mm 3 /N.m (CZ-B0.1) became 0.78 \times 10 $^{-6}$ mm 3 /N.m (CZ-B0.6).
- 4. Contrary to the results of hardness and wear, the corrosion resistance of iCrFeCoB_x coating in 3.5 % NaCl solution decreased with increasing content of B. Although the formation of fine eutectics and Cr-rich borides increase the mechanical properties, The coating galvanic corrosion becomes more severe, leading to a shift in the corrosion process from pitting to intergranular. Therefore, NiCrFeCoBX coating E_{corr} decreased from -0.456~V to -0.895~V, and Icorr increased from $1.256\times10^{-6}~A/cm^2$ to $3.594\times10^{-6}~A/cm^2$.

Funding

The authors declare that no funds, grants, or other support were received during the preparation of this manuscript.

CRediT authorship contribution statement

Zhe Wu: Investigation, Visualization, Writing – review & editing. Morteza Taheri: Writing – original draft, Supervision, Methodology, Investigation. Kourosh Shirvani: Visualization, Software, Formal analysis, Data curation. Edriss Raji: Visualization, Resources, Conceptualization. Mohammad Javad Torkamany: Project administration, Methodology, Formal analysis, Data curation. Reza Taghavi Jelodar: Investigation, Writing – review & editing.

Declaration of competing interest

The authors declare that they have no known competing financial interests or personal relationships that could have appeared to influence the work reported in this paper.

Data availability

Data will be made available on request.

Appendix A. Supplementary data

Supplementary data to this article can be found online at https://doi.org/10.1016/j.matchemphys.2024.129428.

References

- [1] T. Matsuzaka, A. Hyakubu, Y.S. Kim, A. Matsugaki, T. Nagase, T. Ishimoto, T. Nakano, Development of an equiatomic octonary TiNbTaZrMoHfWCr superhigh-entropy alloy for biomedical applications, Mater. Chem. Phys. (2024) 129120
- [2] L. Meijun, L. Xu, C. Zhu, Z. Li, S. Wei, Research progress of high entropy alloy: surface treatment improves friction and wear properties, J. Mater. Res. Technol. 28 (2023) 752–773.
- [3] S. Liu, C. Li, P. Huang, X. Qiao, Y. Wang, S. Zhao, Investigating microstructural and tribological properties of WTaMoHfNi high-entropy refractory alloy applied to GTD-111 superalloy by ultrasonic-assisted laser cladding, Int. J. Refract. Metals Hard Mater. (2024) 106548.
- [4] N. Jahani, M. Reihanian, K. Gheisari, Alloying and corrosion characteristics of FeNiMnCu-based high entropy alloys, Mater. Chem. Phys. (2024) 128990.
- [5] D. Xin, C. Wang, J. Guo, C. Wu, Improved mechanical properties of a near-eutectic high-entropy alloy via laser melting deposition, Mater. Lett. (2024) 136084.
- [6] Y. Lu, Y. Dong, S. Guo, L. Jiang, H. Kang, T. Wang, T. Li, A promising new class of high-temperature alloys: eutectic high-entropy alloys, Sci. Rep. 4 (1) (2014) 6200.
- [7] .
- [8] .
- [9] M. Wang, Z. Wen, J. Liu, B. Ma, M. Wang, Z. Zou, Y. Zhao, Labyrinthine structure AlxCrFeNi (x≥ 1) eutectic high entropy alloys with duplex reinforced phases, J. Alloys Compd. 918 (2022) 165441.
- [10] H. Chang, T.W. Zhang, S.G. Ma, D. Zhao, R.L. Xiong, T. Wang, Z.H. Wang, Novel Siadded CrCoNi medium entropy alloys achieving the breakthrough of strengthductility trade-off, Mater. Des. 197 (2021) 109202.
- [11] X. Jin, J. Bi, L. Zhang, Y. Zhou, X. Du, Y. Liang, B. Li, A new CrFeNi2Al eutectic high entropy alloy system with excellent mechanical properties, J. Alloys Compd. 770 (2019) 655–661.
- [12] H. Jiang, D. Qiao, W. Jiao, K. Han, L. Yiping, P.K. Liaw, Tensile deformation behavior and mechanical properties of a bulk cast Alo. 9CoFeNi2 eutectic highentropy alloy, J. Mater. Sci. Technol. 61 (2021) 119–124.
- [13] S. Zhang, M. Shi, Z. Zhang, W. Quan, Influence of metalloid element B on the microstructure and performances of novel FeCoNiVB high-entropy amorphous alloys, Mater. Lett. 136216 (2024).
- [14] A. Khorram, M. Taheri, M. Fasahat, Laser cladding of Inconel 713 LC with Stellite 31 powder: Statistical modeling and optimization, Laser Phys. 31 (9) (2021) 096001.
- [15] Z. Zuo, M. Taheri, M. Razavi, M.J. Torkamany, A. Rasoulpouraghdam, R. V. Vignesh, Effect of magnetic field on tribological properties of IN718 superalloy coating produced by laser cladding on GTD-111 superalloy, Vacuum 203 (2022) 111311
- [16] H. Zhang, Y. Pan, Y. Zhang, G. Lian, Q. Cao, J. Yang, Influence of laser power on the microstructure and properties of in-situ NbC/WCoB-TiC coating by laser cladding, Mater. Chem. Phys. 290 (2022) 126636.
- [17] Y. Lei, M. Taheri, A.H. Lashkari, P. Torkamany, I. Heidarpour, M.J. Torkamany, Corrosion resistance of NbCrFeNiCoMoX coating applied by laser cladding on GTD-111 superalloy: application of gas turbine blade, Mater. Today Commun. 38 (2024) 108157.
- [18] S. Zhao, M. Taheri, K. Shirvani, M. Naserlouei, K. Beirami, M. Paidar, W. Sai, Microstructure of NbMoTaTiNi refractory high-entropy alloy coating fabricated by ultrasonic field-assisted laser cladding process, Coatings 13 (6) (2023) 995.
- [19] Z. Li, M. Taheri, P. Torkamany, I. Heidarpour, M.J. Torkamany, Laser cladding of NiCrCoFeNbMoX high-entropy alloy to increase resistance to corrosion of gas turbine blades, Vacuum 219 (2024) 112749.
- [20] Y. Deng, Y. Huang, Z. Xu, X. Wang, D. Dong, D. Zhu, T. Ma, Effects of annealing on the mechanical and wear resistance properties of a designed novel eutectic highentropy alloy, J. Alloys Compd. 980 (2024) 173642.
- [21] Z. Li, D. Xie, F. Lv, K. Zhou, C. Jiao, X. Gao, L. Shen, Effect of WC on the microstructure and mechanical properties of laser-clad AlCoCrFeNi2. 1 eutectic high-entropy alloy composite coatings, J. Alloys Compd. 976 (2024) 173219.
- [22] K. Xiang, L. Chai, C. Zhang, H. Guan, Y. Wang, Y. Ma, Y. Li, Investigation of microstructure and wear resistance of laser-clad CoCrNiTi and CrFeNiTi mediumentropy alloy coatings on Ti sheet, Opt Laser. Technol. 145 (2022) 107518.
- [23] K. Chen, Z. Xiong, M. An, Z. Xu, X. Cheng, Large strength and decent ductility at 600° C achieved in bimodal eutectic high-entropy alloys, J. Mater. Res. Technol. 22 (2023) 3436–3441.
- [24] Y. Cao, N. Farouk, M. Taheri, A.V. Yumashev, S.F.K. Bozorg, O.O. Ojo, Evolution of solidification and microstructure in laser-clad IN625 superalloy powder on GTD-111 superalloy, Surf. Coating. Technol. 412 (2021) 127010.
- [25] S. Yan, Z. Li, L. Song, Y. Zhang, S. Wei, Research and development status of laser micro-welding of aluminum-copper dissimilar metals: a review, Opt Laser. Eng. 161 (2023) 107312.
- [26] B. Amanzhulov, I. Ivanov, V. Uglov, S. Zlotski, A. Ryskulov, A. Kurakhmedov, M. Zdorovets, Composition and structure of NiCoFeCr and NiCoFeCrMn highentropy alloys irradiated by helium ions, Materials 16 (10) (2023) 3695.

- [27] W. Al Zoubi, R.A.K. Putri, M.R. Abukhadra, Y.G. Ko, Recent experimental and theoretical advances in the design and science of high-entropy alloy nanoparticles, Nano Energy 110 (2023) 108362.
- [28] Z. Zuo, M. Taheri, M. Razavi, M.J. Torkamany, A. Rasoulpouraghdam, R. V. Vignesh, Effect of magnetic field on tribological properties of IN718 superalloy coating produced by laser cladding on GTD-111 superalloy, Vacuum 203 (2022) 111311.
- [29] M. Taheri, M. Razavi, Effect of TiC on the microstructure of GTD-111 superalloy processed by laser powder bed fusion, Mater. Lett. 328 (2022) 133091.
- [30] Z. Li, Y. Du, G. He, Z. Zhou, Q. Liang, L. Shu, Optimization of the overlap rate of multi-track laser cladding based on the flat-top overlapping model, Trans. Indian Inst. Met. 76 (10) (2023) 2773–2782.
- [31] J. Wang, X. Cui, Y. Zhao, Y. Zhang, X. Fan, M. Zha, G. Jin, Microstructure and performance enhancement of the TiN/Fe-based cladding layer induced by mechanical vibration assisted underwater wet laser cladding, Surf. Coating. Technol. 476 (2024) 130176.
- [32] C.S. Jia, L.H. Zhang, X.L. Peng, J.X. Luo, Y.L. Zhao, J.Y. Liu, L.D. Tang, Prediction of entropy and Gibbs free energy for nitrogen, Chem. Eng. Sci. 202 (2019) 70–74.
- [33] K. Xiang, L.Y. Chen, L. Chai, N. Guo, H. Wang, Microstructural characteristics and properties of CoCrFeNiNbx high-entropy alloy coatings on pure titanium substrate by pulsed laser cladding, Appl. Surf. Sci. 517 (2020) 146214.
- [34] Q. Guo, Y. Pan, H. Hou, Y. Zhao, Predicting the hardness of high-entropy alloys based on compositions, Int. J. Refract. Metals Hard Mater. 112 (2023) 106116.

- [35] Y. He, M. Taheri, Y. Zou, A. Lashkari, K. Shirvani, K. Beirami, A.P. Moghaddam, Investigating the microstructure and tribological properties of ZrB2 and ZrB2/TiB2 coatings applied by ultrasonic field-assisted laser cladding, Mater. Lett. (2024) 136449.
- [36] Q. Wang, J. Shi, L. Zhang, S. Tsutsumi, J. Feng, N. Ma, Impacts of laser cladding residual stress and material properties of functionally graded layers on titanium alloy sheet, Addit. Manuf. 35 (2020) 101303.
- [37] Z. Wang, J. Jin, G.H. Zhang, X.H. Fan, L. Zhang, Effect of temperature on the passive film structure and corrosion performance of CoCrFeMoNi high-entropy alloy, Corrosion Sci. 208 (2022) 110661.
- [38] M. He, H. Kang, G. Hou, Z. Lian, S. Lu, Y. Li, X. Wu, Fabrication of eutectic FeCrCoNiV1. 5 high entropy alloy coating with excellent high-temperature wear resistance, Surf. Coating. Technol. 476 (2024) 130232.
- [39] Y. Yang, X. Li, M.M. Khonsari, Y. Zhu, H. Yang, On enhancing surface wear resistance via rotating grains during selective laser melting, Addit. Manuf. 36 (2020) 101583.
- [40] W. Li, L. Chen, D. Liu, J. Liu, L. An, Ultra-low temperature reactive flash sintering synthesis of high-enthalpy and high-entropy Ca0. 2Co0. 2Nio. 2Cuo. 2Zno. 2O oxide ceramics, Mater. Lett. 304 (2021) 130679.
- [41] L. Chai, C. Wang, K. Xiang, Y. Wang, T. Wang, Y. Ma, Phase constitution, microstructure and properties of pulsed laser-clad ternary CrNiTi medium-entropy alloy coating on pure titanium, Surf. Coating. Technol. 402 (2020) 126503.